

Thermodynamics of alkali feldspar solid solutions with varying Al–Si order: atomistic simulations using a neural network potential

Alexander Gorfer,^{1,2} David Heuser,² Rainer Abart,² and Christoph Dellago¹

¹*Faculty of Physics, University of Vienna, Boltzmanngasse 5, 1090, Vienna, Austria*

²*Department of Lithospheric Research, University of Vienna, Josef-Holaubek-Platz 2, 1090, Vienna, Austria*

The thermodynamic mixing properties of alkali feldspar solid solutions between the Na and K end members were computed through atomistic simulations using a neural network potential. We performed combined molecular dynamics and Monte Carlo simulations in the semi-grand canonical ensemble at 800 °C and considered three quenched disorder states in the Al–Si–O framework ranging from fully ordered to fully disordered. The excess Gibbs energy of mixing, excess enthalpy of mixing and excess entropy of mixing are in good agreement with literature data. In particular, the notion that increasing disorder in the Al–Si–O framework correlates with increasing ideality of Na–K mixing is successfully predicted. Finally, a recently proposed short range ordering of Na and K in the alkali sublattice is observed, which may be considered as a precursor to exsolution lamellae, a characteristic phenomenon in alkali feldspar of intermediate composition leading to perthite formation during cooling.

I. INTRODUCTION

Feldspar, the most abundant mineral in the Earth's crust, is a framework silicate comprised of corner sharing $[\text{SiO}_4]^{-4}$ and $[\text{AlO}_4]^{-5}$ tetrahedra forming a three-dimensional framework with large cavities, which are occupied by cations that balance the net negative charge of the tetrahedral framework. The most common cations with suitable ionic radius and charge to enter these cavities are Ca^{2+} , Na^+ and K^+ , giving rise to the ternary solid solution: $\text{CaAl}_2\text{Si}_2\text{O}_8$ – $\text{NaAlSi}_3\text{O}_8$ – KAlSi_3O_8 . The binary solid solution between $\text{NaAlSi}_3\text{O}_8$ (albite) and KAlSi_3O_8 (K-feldspar) is known as alkali feldspar, which is further classified based on the potassium site fraction on the alkali site X_K and on the degree of disorder in the Al–Si–O tetrahedral framework. Different states of disorder may arise due to the fact that there are four distinct tetrahedral sites: T_{10} , T_{1M} , T_{2O} and T_{2M} (Fig. 1 a). In low-temperature, ordered alkali feldspar, the Al^{3+} cations exclusively occupy the T_{10} sites. At intermediate temperatures, Al^{3+} favors T_{10} and T_{1M} over T_{2O} and T_{2M} , and at high temperatures Al^{3+} is randomly distributed over all the tetrahedral sites.

The disorder phenomena that accompany Na–K mixing on the alkali sublattice and Al–Si mixing on the Al–Si–O framework make alkali feldspar a challenging system in terms of its thermodynamic properties. The Al–Si disorder in particular can take significant timescales to equilibrate, like the fully ordered low microcline in Klokken that took 10^4 to 10^5 years to develop [1]. This means that many laboratory experiments are conducted on essentially quenched states of Al–Si disorder. Therefore, investigations into feldspar thermodynamics must consider T , P , X_K and the state of Al–Si disorder. The latter is typically classified using Kroll and Ribbe's scheme [2], which is based on unit cell dimensions. An accurate understanding of feldspar thermodynamics is key in deducing the thermal history of magmatic and metamorphic rocks from the compositions and microstructures of al-

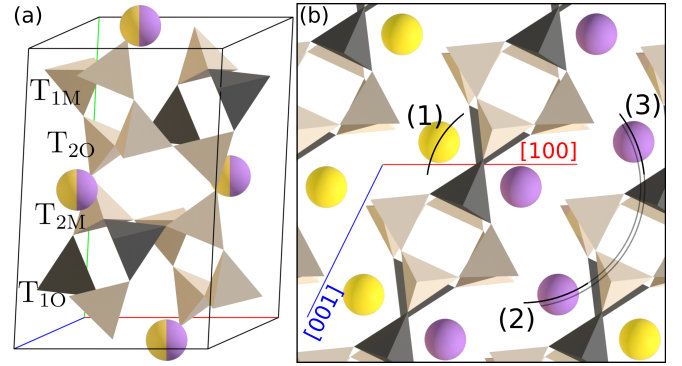


Figure 1. (a) Unit cell of Al ordered alkali feldspar with Al^{3+} at the T_{10} tetrahedra. The Al–Si tetrahedra types are labeled on the leftmost tetrahedra. Na^+/K^+ is illustrated as yellow/purple spheres. In (b) we see the (010) plane and the first three Na–K configuration shells. The Na^+/K^+ distribution shows the SRO we found in an exaggerated fashion.

kali feldspars in exhumed samples.

A recent overview of the current state of knowledge about alkali feldspar thermodynamics can be found in Ref. [3]. Over the years, several authors have performed experiments on the thermodynamics of alkali feldspar. The solvus, which has its T_C around 650 °C to 870 °C, depending on the state of Al–Si disorder and on pressure, was directly determined for various states of Al–Si disorder primarily in the 1960s and 70s but also in 2024 [4–11]. Sodium–potassium partitioning experiments have been performed repeatedly, starting from 1975 and up to 2024 [12–15]. Also measured were mixing enthalpies for different ordering states in [3, 13] and vibrational entropies in [15, 16].

The Al–Si disorder also complicates computational studies, as modeling disorder generally requires large system sizes due to the lack of translational symmetry. This calls for application of computationally inexpensive classical force-fields, which are tuned empirically, such as lat-

tice energy models that have been applied to Al-Si thermodynamics in feldspar [17, 18]. It is, however, desirable to use first-principles methods such as Density Functional Theory (DFT), which can provide higher accuracy with less reliance on human tuning. But due to their computational costs, studies using DFT have either focused on properties of ordered end-members [19–22], or used systems with essentially “hand-made” Na-K disorder with limited realizations of X_K to study the vibrational entropy [23], excess enthalpy of mixing [24] and K-O bond lengths [25]. Other features of alkali feldspar that were obtained by DFT modeling include point defects [26] and the feldspar-water interface [27–29].

To summarize, despite significant effort, the thermodynamics of alkali feldspar remain incompletely understood. Machine Learning Force Fields (MLFF), reviewed in [30], offer a promising pathway towards a better understanding by combining the accuracy of DFT calculations with system scales accessible only to classical force-field methods. Recent studies have already explored the applicability of MLFFs for alkali feldspar, including a neural network potential for Na^+ point defects in albite [26] to study Na-diffusion [31] and, motivated by the ice-nucleating properties of alkali-feldspar, a deep potential for modeling the microcline-water interface [29].

This study investigates the thermodynamic properties of the alkali feldspar solid solution across the full range of Na-K compositions and formally treats disorder for three archetypes:

1. *Al ordered* with $X_{\text{T1O}} = 1$. This ordering is supposed to represent solid solutions between low albite and microcline.
2. *Al T_1 -disordered* with $X_{\text{T1O}} = X_{\text{T1M}} = 0.5$. This ordering is supposed to represent an in-between configuration with Al occupying both $\text{T}_{1\text{O}}$ and $\text{T}_{1\text{M}}$ at random such as may be found in orthoclase.
3. *Al disordered* with $X_{\text{T1}} = 0.25$. This ordering represents the most extreme type of disorder, such as may be found in solid solutions between high albite and sanidine.

We discuss an algorithm for creating specific states of Al-Si and Na-K disorder, the training of a Neural Network Potential (NNP) to simulate their dynamics, and Semi-Grand Canonical Monte Carlo (SGCMC) simulations to calculate equilibrium X_K as a function of chemical potential. The results, which include the excess Gibbs energy of mixing, excess enthalpy of mixing and excess entropy of mixing show good agreement with experimental data, and they also reveal the impact of Al-Si disorder on these excess properties as well as on the solvus. In addition, we observe and quantify a Short Range Ordering (SRO) phenomenon leading to a negative excess configurational entropy and classify it as a precursor to exsolution, which typically occurs in alkali feldspar of intermediate composition during cooling and leads to characteristic lamellar intergrowth of Na-rich and K-rich alkali feldspar referred to as *perthite*.

II. METHODS

A. Na-K short range order

To quantify the degree of Na-K disorder within the alkali sublattice, we use Warren-Cowley Short Range Order (SRO) parameters

$$\alpha_{\text{NaK}}^{(l)} = 1 - \frac{Z_K^{(l)}}{Z_{\text{tot}}^{(l)} X_K}. \quad (1)$$

These are calculated for every Na ion, where $Z_K^{(l)}$ is the instantaneous number of K ions within the l -th configuration shell, $Z_{\text{tot}}^{(l)}$ is the total number of neighbors in the l -th shell, and X_K is the overall K site fraction of K on the alkali sublattice. In a completely random alloy, the expected number of K neighbors for an Na would be $Z_{\text{tot}}^{(l)} X_K$ and $\alpha_{\text{NaK}}^{(l)} = 0$. If $\alpha_{\text{NaK}}^{(l)} > 0$, there is a tendency for Na and K ions to cluster, while for $\alpha_{\text{NaK}}^{(l)} < 0$ there exists an ordering where Na ions have more K neighbors than expected by chance. In Fig. 1 (b) the first three Na-K configuration shells are illustrated. Due to their similarities, for the second and third nearest neighbors we calculate an $\alpha_{\text{NaK}}^{(2-3)}$ as if they were on the same shell.

B. Treating Al-Si and Na-K disorder in alkali feldspar

As discussed in the Introduction, the state of Al-Si disorder in the tetrahedral framework may be a complicated function of temperature, pressure as well as potassium site fraction, but the slow ordering of the Al-Si [32, 33] allows, or more appropriate, forces experiments to be done with a quenched Al-Si order on laboratory timescales. While this is less true at and above certain temperatures and timescales where Al-Si disordering is reported [15, 34], since our aim is to best emulate usual experimental conditions, it is reasonable to assume a state of quenched Al-Si disorder that does not change throughout the simulation.

Atomistic simulations of disordered systems require large system sizes as the translational symmetry is broken. For first-principle electronic structure calculations with DFT, where computational cost scales with the third power of the number of electrons, these system sizes are prohibitively expensive and have only recently been investigated using specific pre-defined configurations of Na-K disorder by Benisek and Dachs [23, 24] and by Li et al. [25].

We propose an algorithm to generate well-defined configurations of disordered alkali feldspars. Below is its pseudocode, but we also give an explanation in prose.

The algorithm takes as input the potassium fraction X_K , the Al-fractions at each of the different tetrahedral sites $\{X_{\text{T1O}}, X_{\text{T1M}}, X_{\text{T2O}}, X_{\text{T2M}}\}$, the supercell dimen-

sion in each direction a, b, c and a parameter that controls the Na-K distribution scheme.

Algorithm Alkali feldspar disorder generation scheme

Require: Fractions $X_K, X_{T1O}, X_{T1M}, X_{T2O}, X_{T2M}$ and integer supercell dimensions a, b, c and bool NaK-SQS

- 1: Create supercell configuration with dimensions a, b, c .
 - 2: Distribute Al among possible tetrahedra at random.
 - 3: Swap Al with Al neighbors with Si without any Al neighbors to fulfill Loewenstein’s rule.
 - 4: **while** $X'_{Ti} \neq X_{Ti}$ **do**
 - 5: move Al from site with $X'_{Ti} > X_{Ti}$ to site with $X'_{Ti} < X_{Ti}$.
 - 6: **if** NaK-SQS **then**
 - 7: Distribute Na-K according to SQS.
 - 8: **else**
 - 9: Distribute Na-K at random.
 - 10: **return** configuration
-

To create Al-Si disorder, the aluminum is distributed randomly across all Al-Si tetrahedra with non-zero Al-fraction. Adherence to Loewenstein’s rule, which prohibits adjacent Al tetrahedra and is assumed to be well fulfilled in alkali feldspar, is maintained by iteratively swapping an Al that neighbors an Al by an Si that is surrounded exclusively by Si. The algorithm then compares the instantaneous Al-fractions (X'_{Ti}) with the input values and continuously swaps Al and Si, adhering to Loewenstein’s rule, until the desired Al-fractions are reached. At *unreasonable* input Al-fractions such as $X_{T1M} = X_{T2M} = 0.5$, $X_{T1O} = X_{T2O} = 0$ we observed that it is possible for the algorithm to get stuck in a configuration and allow a random move to get out, but for realistic Al-disorder states and in particular for all disorder states treated in this work, this is not necessary.

To generate a disordered alkali-sublattice we either just distribute Na-K at random, or we distribute them according to Special Quasirandom Structures (SQS). In the latter scheme, the Na-K configuration is optimized to get $\alpha_{Na}^{(I)}$ as close to zero as possible. Using SQS speeds up the convergence of self-averaging properties with increasing system-sizes. Our Python implementation, openly available on GitHub, employs the sqsgenerator package [35] to generate SQS and optimizes using the first 10 shells. It also uses the ASE package [36] to represent atomic configurations.

In this study we consider the three types of archetypical Al-Si disorder that are defined in the Introduction: Al ordered, Al T_1 -disordered and Al disordered.

The literature offers algorithms in which the Al-disorder configuration results from simulations using empirical lattice energy models [17, 18]. While the result of these modeling approaches can be expected to offer higher realism in the Al-Si disorder configurations, in this study we wanted to rely on a purely first-principles methodology such that we refrained from using empirical force-fields to create the Al-Si ordering and we also wanted to create a baseline of extreme ordering

archetypes that future investigations may build upon.

C. Ab initio calculations

To train and test the NNP, with which we ultimately run large-scale (19 968 atoms) simulations, we performed smaller-scale (~ 416 atoms) DFT calculations using the Vienna Ab initio Simulation Package (VASP) [37–39] with the projector augmented wave method [40] using the Perdew-Burke-Ernzerhof (PBE) [41] exchange correlation functional. We used identical settings and convergence criteria as in Ref. [26], allowing us to reuse the associated dataset of that study [42]. When charged point defects are included in the supercell, we varied the number of electrons using a jellium background and included the point-charge electrostatic correction to the potential energy to correct for finite-size electrostatic effects (see SM for details).

D. Neural network potential and training/testing datasets

We developed a Neural Network Potential (NNP) that can treat Al-Si disorder, mixtures of Na-K as well as the following point-defects: Na-Na-dumbbell, Na-(0, 0, $\frac{1}{2}$)-interstitial, Na-K-dumbbell, Na-vacancy and K-vacancy (see [26] for nomenclature), although the point defects are immaterial to this study. Our NNP uses the architecture of Behler and Parrinello [43].

The local atomic environments are represented by radial symmetry functions and two classes of angular atom-centered symmetry functions. For angles involving O, we use both the narrow and wide angular symmetry functions given in Ref. [44]. To also describe all other possibilities, we use weighted atom-centered angular symmetry functions (wACSF) [45]. Unlike [45], to discern between different chemical elements, our wACSFs use the Pauling electronegativity instead of the atomic number as variables in the element-dependent weighting function h (see the SM for details). The input layer of the feed forward networks, consisting of the symmetry functions, has a length of 213 for the case of O, 209 for Al, 210 for Si, 211 for Na and 205 for K. This is followed by two hidden layers with 25 nodes each and a single output node. We trained four potentials with random initial weights using the n2p2 package [46], optimizing the root mean squared error via a parallel Kalman-filter [47] and combine them in a committee machine using the n2p2-committee implementation given in Ref. [48].

To construct the training and testing datasets we first reused the training set constructed in Ref. [26] for Na-feldspar, except that we apply the point-charge electrostatic correction instead of the correction of Kumagai and Oba (see SM). We then also employed the on-the-fly approach described in [26] using the on-the-fly learning implementation of VASP [49, 50] for a hand-made Na-K

mixed $2 \times 1 \times 2$ supercell containing 13 K and 3 Na, both with and without an Na^+ -interstitial. The combined dataset was used to create a preliminary NNP committee, which we iteratively refined through an active-learning scheme similar to Ref. [26] by incorporating uncertain configurations encountered during MD simulations. The differences from Ref. [26] are the supercell sizes, which are $2 \times 1 \times 2$, the variation of the Na-K distribution covering X_K from 0.0 to 1.0, the use of hand-made Al-Si disorder realizations and the use of the aforementioned point-defects. After repeating this 10 times, creating different disorder realizations in each iteration, we had a training set of 4657 structures as well as a hyperparameter-optimized and stable force-field. We then used our algorithm to further expand the dataset using systematically generated structures: $2 \times 2 \times 2$ supercells with Al disorder were generated for potassium fractions $X_K = \{0.1, 0.2, \dots, 0.9\}$, where for each X'_K , 10 different Al-Si and Na-K disorder realizations were generated (90 defect-free realizations in total). The NaK-SQS scheme was omitted, as we wanted to cover all possible local motifs. In these systems, the 5 defect-types were introduced separately (540 initial systems). These were fully relaxed to create 0 K configurations. Subsequently, for each X'_K , 6 realizations including the defect-free and the defective systems were simulated using NPT-MD at 600 K, then 1000 K and continuing at 1400 K. Each temperature was simulated for 60 ps and configurations at 20, 25, \dots 60 ps were saved (regardless of committee uncertainty). Configurations from 2 realizations per X'_K , which were simulated using NPT-MD, were used to build a test set containing 1667 structures, while the rest were added to the training set which includes 8720 structures in total.

E. Neural network potential performance

The NNP was tested on a set containing 1667 Al disordered structures covering $X_K = \{0.1, 0.2, \dots, 0.9\}$ and the defects: Na-Na-dumbbell, Na-(0, 0, $\frac{1}{2}$)-interstitial, Na-K-dumbbell, Na-vacancy and K-vacancy as well as the defect-free system for temperatures 0, 600, 1000 and 1400 K. The specific realizations of Na-K and Al-Si disorder states that are tested are not included in the training set to test the ability to generalize to new unseen configurations. The potential performs well over the whole dataset as can be seen from the root mean squared errors (RMSE) and mean average errors (MAE) shown in Tab. I and errors for each configuration separately in Fig. 2.

Table I. Energy and force RMSE and MAE for the test set.

	ΔE [$\frac{\text{meV}}{\text{atom}}$]	ΔF [$\frac{\text{eV}}{\text{\AA}}$]
RMSE	0.84	0.12
MAE	0.63	0.08

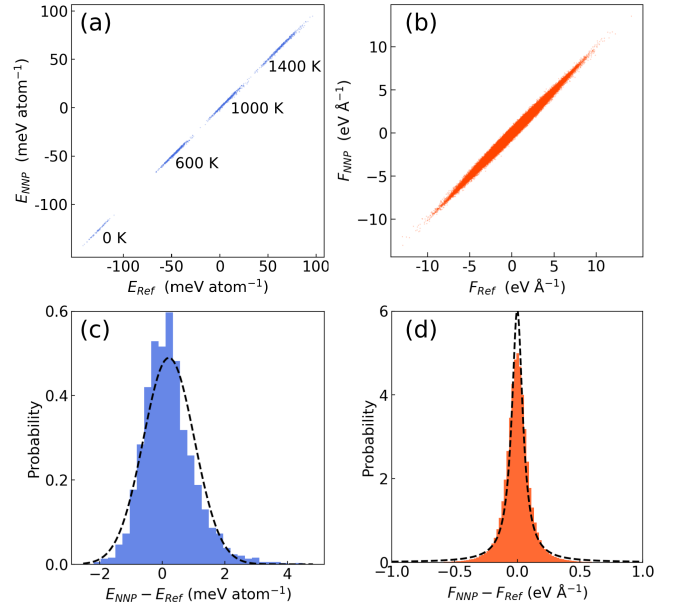


Figure 2. (a) Energy parity plot for the test set showing the neural network potential (NNP) versus the DFT reference. The axes were centered at zero. The four different temperatures sampled in the test set can be seen. (b) parity plot for the force predictions. The error distributions are shown in the second row. For energy errors (c) a normal distribution is overlain, for force errors (d) a Cauchy distribution is shown instead.

F. Unit cell minimization

To determine the equilibrium 0 K unit cell parameters we used our algorithm to generate supercells with dimensions $8 \times 6 \times 8$ (i.e. 19968 atoms) for the three Al-Si disorder states covering $X_K = \{0, 0.1, \dots, 1\}$ with NaK-SQS enabled. Each system was then fully relaxed in LAMMPS [51] by iterating between purely ionic relaxations and relaxations of both ionic and box degrees of freedom (DOF). Both minimizations consisted of a conjugated gradient descent followed by a steepest gradient descent (SGD). The purely ionic SGD always reached the energy threshold of 1×10^{-12} eV, whereas initially, the ionic plus box DOF SGD had to be preemptively terminated after a maximum of 3000 steps was reached. Iterations between purely ionic and ionic plus box DOF relaxations were repeated until the energy difference between the final configuration and the next-to-last box-DOF SGD relaxed structure was less than 0.01 eV or 6.3×10^{-4} kJ mol $^{-1}$ for all structures. The disordered systems with $X_K = 0.0$ required the longest with around 30 iterations to reach this convergence level. Input files are available in the Zenodo repository [52].

G. Miscibility calculations using SGCMC-MD

To determine mixing thermodynamics at finite temperature we simulated alkali feldspar using Molecular Dynamics (MD) together with Semi-Grand Canonical Monte Carlo (SGCMC), implemented within LAMMPS [51, 53]. The SGCMC approach allows alchemical transformations from Na to K as well as K to Na that are accepted with a probability [53]:

$$P_{\text{acc}} = \min\{1, \exp[-\beta(\Delta U + \Delta\mu N\Delta X_K)]\},$$

where ΔU is the change in potential energy before and after alchemical swapping, ΔX_K is the change in potassium site fraction and $\Delta\mu \equiv \mu_{\text{Na}} - \mu_{\text{K}}$ is the difference in chemical potential between K and Na which is set before every simulation. Aiming to cover the whole range of Na-K compositions, we identified the following suitable values of $\Delta\mu = \{-1, -0.05, -0.0375, -0.03125, -0.028125, -0.0265625, -0.025, -0.021875, -0.01875, -0.0125, -0.00625, 0, 0.0125\}$ (eV) by trial and error.

For each Al-ordering state and $\Delta\mu$ value, a relaxed $8 \times 6 \times 8$ supercell was first equilibrated in the SGC-PT ensemble at 1073.15 K and atmospheric pressure. A single realization of Al-ordering was used for each of the three Al-ordering archetypes. The damping parameters were 0.1 ps for the Langevin thermostat and 1 ps for the Nose-Hoover barostat. The timestep of the dynamics was 1 fs. Initially, 5000 MC moves were attempted every 400 timesteps. After 4×10^5 MC attempts, the frequency was reduced to 250 attempts per 400 timesteps and the equilibration was continued for an additional 5×10^5 attempts. Subsequently, while maintaining these parameters, configurations including the chemical identity for every atom, the potential energy and volume was written to disk every 400 timesteps at exactly one timestep before the MC moves. These production runs were conducted for an additional 7×10^5 MC attempts, lasting around 1.1 ns. The enthalpy of the end-members was calculated in the NPT ensemble without SGCMC using the aforementioned thermo- and barostat.

The acceptance ratio depends on $\Delta\mu$. While it was essentially zero at -1 eV, at -0.021875 eV it was 27%. We note that we also attempted MC moves involving swaps between Al and Si, but no moves were ever accepted even for a trial run at 1400 K, implying that the local environment of Al and Si is too different for a sufficient acceptance probability. This is unfortunate as a working SGCMC simulation methodology for the Al-Si sublattice would allow us to calculate the equilibrium Al-Si disorder states, in similarity to Dubacq [18].

III. RESULTS AND DISCUSSION

A. Crystal symmetry

We used fully relaxed supercells (dimensions $8 \times 6 \times 8$, 19968 atoms) to determine the unit cell parameters across

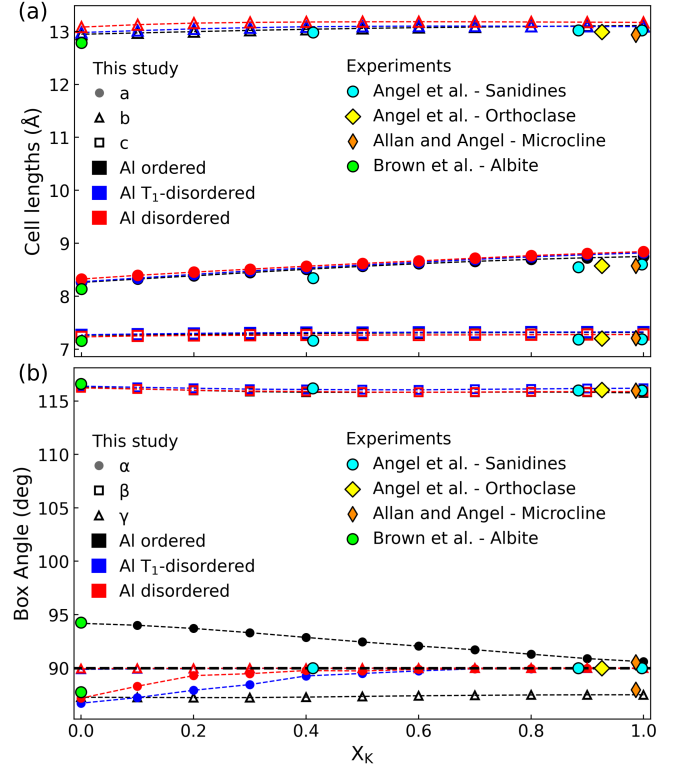


Figure 3. Compositional dependence of the unit cell parameters for the three different states of aluminum order-disorder. With increasing potassium site fraction X_K , the solid-solution becomes successively more monoclinic. For the fully ordered Al-Si framework, the crystal is triclinic for all X_K . For both the T_1 -disorder and the fully Al disordered system the angle $\alpha \leq 90$ deg implies triclinic symmetry at $X_K \leq 0.3$ transitioning to monoclinic symmetry towards higher X_K . We compare with experiments of Angel et al. [54], Allan and Angel [55] and Brown et al. [56].

the entire range of potassium site fractions X_K for the three ordering states defined in the Introduction.

Alkali feldspar transitions between triclinic and monoclinic symmetry, depending on temperature, the state of Al-Si disorder and potassium site fraction X_K . For monoclinic symmetry, $\alpha = \gamma = 90$ deg. The compositional dependence of α , β and γ is shown in Fig. 3 (b). For high and intermediate states of Al-Si disorder the crystal structure is triclinic for Na-rich compositions and approaches monoclinic symmetry with increasing potassium site fraction, a trend that is consistent with experimental observations. The ordered system never reaches monoclinic symmetry even at $X_K = 1$, which aligns with the behavior of microcline, fully ordered K-feldspar. The two Al-Si disordered systems are much closer to the monoclinic symmetry overall and are fully monoclinic at $X_K \geq 0.4$. The differences between the Al T_1 -disorder and the full disorder are subordinate.

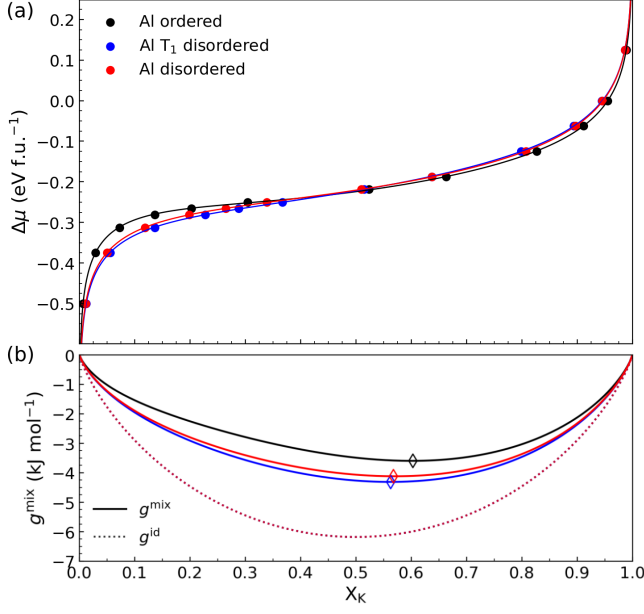


Figure 4. (a) Difference in chemical potential $\Delta\mu = \mu_{\text{Na}} - \mu_{\text{K}}$ versus equilibrium composition X_K of alkali feldspar for the three states of Al-Si disorder at 1073.15 K. The definitive integral of $\Delta\mu(X_K)$ and subtraction of the linear dependence yields the Gibbs energy of mixing g^{mix} shown in (b). The extrema are shown as diamonds and the Gibbs energy of mixing of an ideal mixture g^{id} is shown as a dotted line.

B. Miscibility and non-ideality

The results of the SGCMC-MD simulations are shown in Fig. 4. In (a) the relationship between chemical potential difference $\Delta\mu$ and the equilibrium K concentration X_K is presented for the three states of Al-Si disorder. The shapes of the curves indicate that the non-ideality is more pronounced for the Al-Si ordered state than for the two disordered ones. The latter two align closely, with the Al T₁-disordered state being slightly more ideal. The results from SGCMC modeling are similar to the equilibrium partitioning experiments between alkali feldspar and a NaCl-KCl salt melt, which yields the equilibrium X_K site fraction of alkali feldspar as a function of melt composition as expressed by its molar KCl fraction [15].

Figure 5 shows the excess properties of mixing. The enthalpy of mixing h^{ex} in (a) was determined from the potential energies and volumes sampled during the SGCMC-MD simulations at 1073.15 K, as well as from the potential energy of the fully relaxed systems at 0 K. We can see that introducing Al-Si disorder leads to more ideal values as the maximum is shifted almost 2.5 kJ mol.⁻¹ lower at 1073.15 K and between 1 to 2 kJ mol.⁻¹ lower at 0 K. This observation holds for both Al-Si disordered states, which show remarkable agreement at high temperatures. Possibly, the excess enthalpy decreases when Al distributes on both T_O- and T_M-tetrahedra, regardless of whether these fall under the

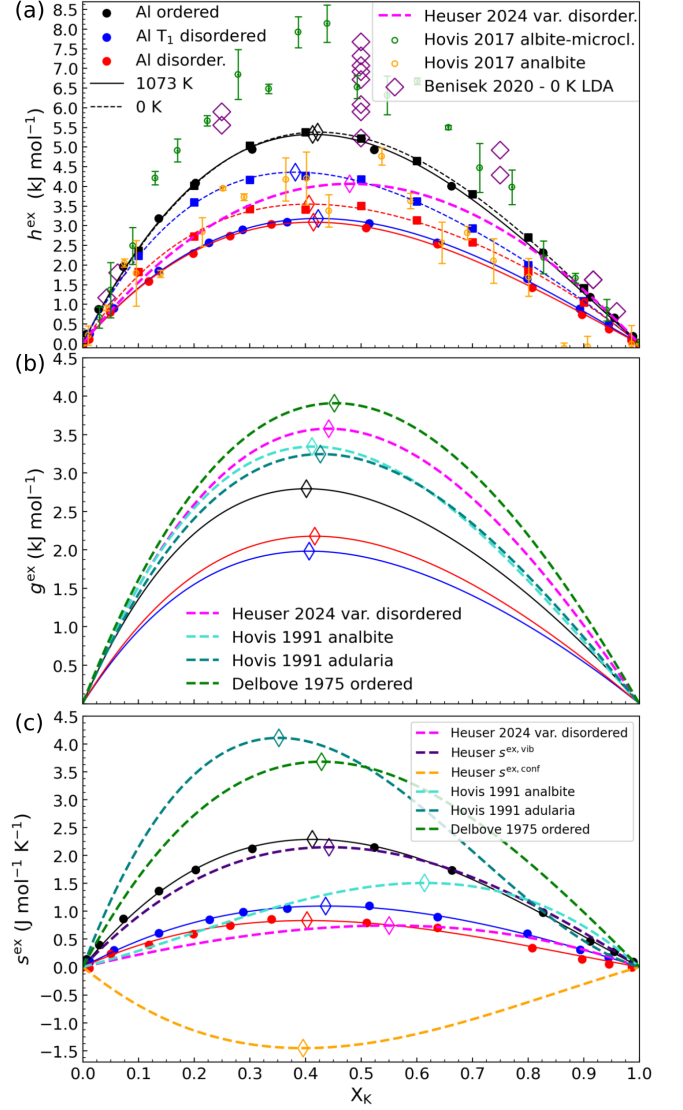


Figure 5. Excess properties of mixing versus composition for the different states of Al-Si disorder. The results of this study are in black/blue/red for the Al-Si ordered/T₁-disordered/disordered systems. (a) shows the excess enthalpy of mixing h^{ex} sampled over the simulations at 1073.15 K and at 0 K (dashed). In (b) the excess Gibbs energy of mixing g^{ex} obtained from Fig. 4 (b) is shown. (c) shows the excess entropy of mixing $s^{\text{ex}} = (h^{\text{ex}} - g^{\text{ex}})/T$. Diamonds locate the extrema. Curves in (a) and (c) are the Margules fit to our results. We compare with experiments of Heuser et al. [15] (1073.15 K), Hovis 2017 [3] (323.15 K) for ordered h^{ex} (albite-microcline) and disordered h^{ex} (analbite), LDA calculations of Benisek and Dachs [24] (0 K) for ordered h^{ex} , Hovis et al. 1991 [13] (1073.15 K) for disordered (adularia) and medium-disordered (analbite) g^{ex} and s^{ex} and Delbove [12] (1073.15 K) for ordered g^{ex} and s^{ex} .

T₁ or the T₂ grouping. As temperature increases, the solution becomes more ideal as evidenced by a decrease in h^{ex} . This effect depends significantly on the state of Al-Si disorder, with the Al-Si ordered state exhibiting al-

most no and the Al T_1 disordered state the largest shift. The location of the maximum remains constant at around $X_K = 0.41$ for all h^{ex} curves.

Let us contextualize these results of h^{ex} . Our disordered h^{ex} calculations agree quite well with the 2017 experiment of Hovis [3] on analbite (disordered albite) over the entire compositional range. Also the h^{ex} determined by Heuser and coworkers [15] for various kinds of Al-disordering using the same conditions (1073.15 K and 1 atm) is in a similar range to Hovis. For the case of ordered alkali feldspar we can compare with Hovis's albite-microcline. At close to end-member compositions our calculations are in good agreement with the experimental data, but between 0.2-0.8 the experimental h^{ex} is significantly underestimated. In a recent study by Benisek and Dachs [24] h^{ex} at 0 K was calculated using the same methodology, the only difference being the use of DFT directly, albeit using a different functional; a local-density approximation (LDA) instead of a generalized gradient ascent (GGA) with which we trained our NNP on. The substantially smaller system sizes that are accessible for direct application of DFT result in a large spread and only the Al-ordered system was studied. Nonetheless, the result of Benisek and Dachs seems to be in slightly better agreement with the experiment of Hovis on the albite-microcline h^{ex} than our Al ordered ones, but also underestimating the data. Noteworthy is also that away from the maximum, the data of Heuser and coworkers seems to closely match our disordered h^{ex} at low X_K and with our ordered h^{ex} at high X_K .

The definitive integral of $\Delta\mu(X_K)$ yields the Gibbs energy of mixing plotted in Fig. 4 (b). Subtracting the Gibbs energy of an ideal mixture $g^{\text{id}}(X_K)$ gives the excess Gibbs energy of mixing $g^{\text{ex}}(X_K)$, which is shown in Fig. 5 (b). The maxima of all three ordering states closely align between $X_K = 0.40$ to 0.41 . This is well in line with the broader literature [3], which give a maximum between 0.38 and 0.44. However, our absolute g^{ex} values are about 1 kJ mol^{-1} below the experimental findings. An important feature is the effect of the state of Al-Si disorder on g^{ex} . The experimental data is inconclusive regarding this. While the experiment of Heuser and coworkers, which included a range of Al-Si disordered states, found no difference in excess Gibbs energy of mixing, a collection of investigations covering a broader range of states of Al-Si disorder including Al-Si ordered states does suggest an increase of excess Gibbs energy of mixing with increasing Al-Si order. Our data may offer an explanation: g^{ex} is markedly higher for the Al-Si ordered case (consistent with Hovis [3]), but the two Al-Si disordered states are almost equivalent (consistent with Heuser et al. [15]), suggesting that the g^{ex} primarily depends on the existence of Al-Si disorder but less so on the specific T_1 - T_2 state of this disorder, which is similar to what we found for h^{ex} .

Finally, the excess entropy of mixing $s^{\text{ex}} = (h^{\text{ex}} - g^{\text{ex}})/T$ was calculated and is shown in Fig. 5 (c). The maxima are located between $X_K = 0.40$ to 0.42 . For the

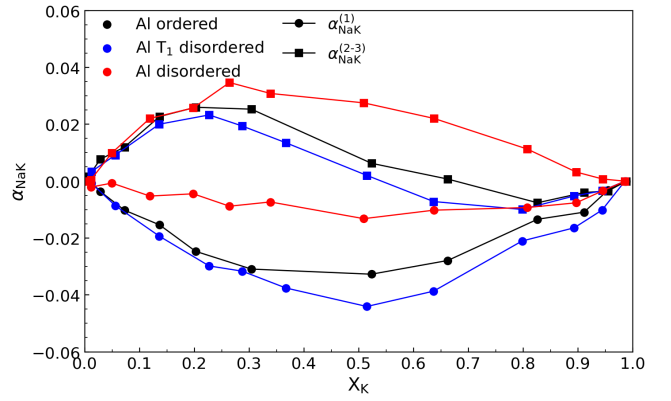


Figure 6. Short range order parameters for the different ordering states.

case of disorder the s^{ex} fit Heuser et al. [15] quite well. In our data the s^{ex} increases with increasing order. It is not clear from the experiments, whether this should be expected as s^{ex} of the low albite-microcline of Delbove [12] is certainly higher than the s^{ex} for the various disordered specimen but the 1991 data of Hovis and coworkers [13] on adularia (intermediate disorder) reaches very high s^{ex} which contrasts with Heuser [15].

C. Short range order

We calculated the Warren-Cowley SRO parameters $\alpha_{\text{NaK}}^{(l)}$ for the first three alkali coordination shells illustrated in Fig. 1 (b) using Eq. 1 and show the result in Fig. 6. The second and third coordination shell are treated as if they were one shell due to their similarities. The shells exhibit opposite coordination tendencies: $\alpha_{\text{NaK}}^{(1)} < 0$ indicating fewer Na-Na nearest neighbors than expected for a random distribution, while $\alpha_{\text{NaK}}^{(2-3)} > 0$ indicating a surplus of Na-Na next nearest neighbors.

This Na-K arrangement is illustrated in an exaggerated fashion in Fig. 1 (b). We can see that, were the $\alpha_{\text{NaK}}^{(1)}$ and $\alpha_{\text{NaK}}^{(2-3)}$ at their maximum values, we would see Na-K lamellae parallel to the (100) plane. This orientation is similar (off by around 24 deg) to the perthite lamellar intergrowth that forms along (-801) to (-601), in which also long-range elastic interactions play a role [57], which we do not expect to influence the SRO. We therefore consider the SRO as a precursor to the perthite lamellae. That a certain SRO can be thought of as a precursor (or remnant) of the low-temperature long-range-ordered phase happens frequently in binary alloys [58] such as $\text{Cu}_{1-x}\text{Au}_x$ [59].

The SRO parameters, although small, are not negligible, especially considering the high temperature. For comparison, Muzyk et al. [60] reported minimum $\alpha_{\text{WV}}^{(1)}$ and $\alpha_{\text{WV}}^{(2)}$ values of around -0.12 and -0.08 , respectively, for tungsten-vanadium alloys at 1000 K and associated

these with non-ideal mixing properties. The non-zero SRO parameters in our study similarly imply excess mixing properties in alkali feldspar, even at high temperatures. Our results also indicate a slightly stronger ordering at $X_K < 0.5$ as compared to more K-rich compositions, consistent with the excess configurational entropy determined by Heuser et al. [15] shown in Fig. 5 (c).

To give a rough estimate of $s^{\text{ex, conf}}$ from our SRO we assume that the alloy-solution model is applicable to the alkali sublattice. Then, we can follow a method summarized by Swalin [61] and express the excess configurational entropy as

$$s^{\text{ex, conf}} = |\alpha| k_B N_A [X_K \ln(X_K) + (1 - X_K) \ln(1 - X_K)],$$

where α is a Warren-Cowley type SRO parameter. For Al T_1 disordered at $X_K = 0.51$ our $\alpha = -0.04$ and we obtain $s^{\text{ex, conf}} = -0.23 \text{ J K}^{-1} \text{ mol}^{-1}$ which is significant in light of a value of s^{ex} of less than $1.1 \text{ J K}^{-1} \text{ mol}^{-1}$ at the same Na-K composition (cf. Fig. 5 c).

A direct quantitative comparison with Heuser et al.'s result is not possible. This is because they determined $s^{\text{ex, conf}}$ by subtracting the excess vibrational entropy $s^{\text{ex, vib}}$ determined at 298.15 K from the total s^{ex} . The values of both $s^{\text{ex, conf}}$ and $s^{\text{ex, vib}}$ are expected to shift at high temperatures, with clustering being canonically much more prevalent at low temperatures.

D. Solvus

Using Margules parameters fitted to the h^{ex} and s^{ex} of Fig. 5 (a, c) (see Table II and the SM), we calculated the strain-free solvus for the three ordering states. The results are shown in Fig. 7.

All three calculated solvi have a critical point between $X_K = 0.32$ to 0.33 which aligns well with the experimentally determined solvi of Heuser et al. [15] at $X_K = 0.37$ and of Bachinski and Müller [6] at $X_K = 0.27$. The critical temperature T_C of the ordered solvus is much higher at 645°C compared to 411°C and 432°C for the disordered ones.

Our ordered solvus is similar to the recently experimentally determined strain-free solvus of Heuser et al. [15], which was determined using mixing thermodynamics at 800°C to 1000°C and 1 atm. Their solvus however represents a range of Al-Si disordered states, and is in agreement with other solvi on disordered alkali feldspars [4, 5, 7] which even though determined at 100 MPa, give a similar result. Bachinski and Müller [6] determined the solvus for the Al-Si ordered low albite-microcline series, albeit at 100 MPa, and their T_C lies 240°C above our ordered solvus. The T_C shift between the ordered Bachinski and Müller and disordered Heuser et al. is marginally smaller at about 211°C , which is predicted extremely well in the shift between our ordered and our disordered T_C of 212 to 233°C .

In our opinion, the fact that our solvi reproduce the temperature shift between ordered and disordered T_C so

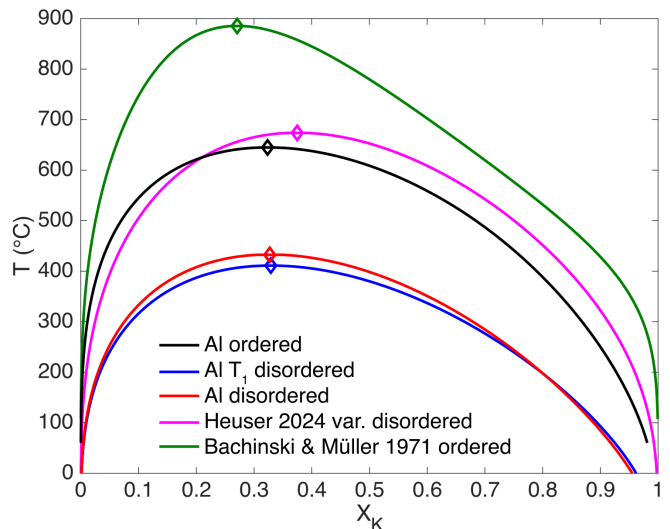


Figure 7. Strain-free solvi of alkali feldspar for the three states of Al-Si disorder and the experiment of Heuser et al. [15], in both cases determined at 1 atm as well as the experiment of Bachinski and Müller [6] for low albite-microcline determined at 100 MPa.

Table II. Margules parameters of the three Al-Si ordering states for the excess enthalpy of mixing W_h (kJ mol^{-1}) and for the excess entropy of mixing W_s ($\text{J mol}^{-1} \text{K}$) determined from the 1073.15 K data of Fig. 5.

	$W_{h\text{Na}}$	$W_{h\text{K}}$	$W_{s\text{Na}}$	$W_{s\text{K}}$
Al ordered	12.75	28.43	5.41	12.27
Al T_1 disordered	8.30	16.52	3.15	5.44
Al disordered	7.48	16.44	1.79	4.59

well, may actually suggest the good agreement of our Al ordered solvus with the solvus of Heuser et al. [15] to be coincidental. In Fig. 5. (a, b) we saw that our methodology seems to underestimate the excess mixing properties, but in a way that keeps the effect of Al-Si disordering consistent with the effects observed in experiments. Overall, Figures 4 and 5 already suggested that the difference between the Al ordered and disordered states is much bigger than between the various states of disordering. This seems to also be the case for the solvi of Fig. 7, as a large temperature shift in T_C is observed between ordered and disordered in both experiment and simulation, which appears to be less sensitive to variations in the degree of Al-Si disorder as long as disorder prevails.

IV. CONCLUSIONS

The feldspar solid solution poses a formidable challenge to both experiments and simulations. We have demonstrated how effects of both Al-Si disorder and Na-K composition can be formally treated starting from first principles. We developed an algorithm that can create

alkali-feldspar systems with certain types of Al-Si disorder which, combined with the construction of a neural network potential, allowed us to probe the impact of Al-Si disorder on the Na-K mixing thermodynamics. Excess mixing properties are in good quantitative agreement, and particularly the effects of Al-Si disorder to the excess mixing properties is in great qualitative agreement with past experiments with disorder resulting in a more ideal mixture and the solvus to shift to lower temperatures as compared to Al-Si ordered configurations. Concurrently, the differences between intermediate and full Al disorder seems to be much less pronounced than between ordered and disordered.

Our simulations offer direct evidence for short range ordering of Na-K which may explain a negative contribution to the configurational entropy measured recently [3, 15]. Interestingly, the Warren-Cowley short range order parameter of the first shell $\alpha_{\text{NaK}}^{(1)}$ is less than 0 whereas $\alpha_{\text{NaK}}^{(2-3)}$ is greater than 0, such that we predict the nearest neighbors to be anticonnected and the ones further away to be clustered. In an exaggerated fashion, Fig. 1 (b) illustrates that such an ordering goes toward Na-K lamellae parallel to the (100)-plane. Since this is likely as close as SRO can get to the actual perthite lamellae, which are oriented between (-801) and (-601), we consider the short range ordering as a precursor of

perthitic lamellar intergrowth.

V. ACKNOWLEDGMENTS

We would like to thank Lukáš Kývala for suggesting to use χ in the wACSF. We acknowledge the financial support from the Austrian Science Fund (FWF) through Grant-DOI 10.55776/I4404 and through Grant-DOI 10.55776/F81. For open access purposes, the author has applied a CC BY public copyright license to any author accepted manuscript version arising from this submission. The computational results presented were achieved using the Vienna Scientific Cluster (VSC).

VI. DATA AVAILABILITY

The algorithm to create Al-Si and Na-K disordered alkali feldspar structures is available as a Python implementation on the GitHub repository <https://github.com/alexgorfer/Alkali-feldspar-disorder-generator>. The LAMMPS-data files of the relaxed $8 \times 6 \times 8$ systems, a template input file for the minimization and for the SGCMC-MD simulation, the training and testing data with and without the point charge correction, the NNP and an n2p2 fork to use the special wACSF to run the NNP are available through the Zenodo repository [52].

-
- [1] W. L. Brown and I. Parsons, Exsolution and coarsening mechanisms and kinetics in an ordered cryptoperthite series, *Contributions to Mineralogy and Petrology* **86**, 3 (1984).
 - [2] H. Kroll and P. H. Ribbe, Determining (Al,Si) distribution and strain in alkali feldspars using lattice parameters and diffraction-peak positions; a review, *American Mineralogist* **72**, 491 (1987).
 - [3] G. L. Hovis, A refined view of the thermodynamic mixing quantities for alkali feldspars and the quandary of excess configurational entropy, *American Journal of Science* **317**, 597 (2017).
 - [4] P. M. Orville, Alkali ion exchange between vapor and feldspar phases, *American Journal of Science* **261**, 201 (1963).
 - [5] W. C. Luth and O. F. Tuttle, The alkali feldspar solvus in the system $\text{Na}_2\text{O}-\text{K}_2\text{O}-\text{Al}_2\text{O}_3-\text{SiO}_2-\text{H}_2\text{O}$, *American Mineralogist: Journal of Earth and Planetary Materials* **51**, 1359 (1966).
 - [6] S. W. Bachinski and G. Müller, Experimental determinations of the microcline—low albite solvus, *Journal of Petrology* **12**, 329 (1971).
 - [7] P. Smith and I. Parsons, The alkali-feldspar solvus at 1 kilobar water-vapour pressure, *Mineralogical Magazine* **39**, 747 (1974).
 - [8] J. R. Goldsmith and R. C. Newton, An experimental determination of the alkali feldspar solvus, in *The Feldspars: Proceedings of a NATO Advanced Study Institute* (Manchester University Press, Manchester, England, 1974) pp. 337–359.
 - [9] M. Lagache and A. Weisbrod, The system: Two alkali feldspars-KCl-NaCl-H₂O at moderate to high temperatures and low pressures, *Contributions to Mineralogy and Petrology* **62**, 77 (1977).
 - [10] I. Parsons, Alkali-feldspars: Which solvus?, *Physics and Chemistry of Minerals* **2**, 199 (1978).
 - [11] D. Heuser, R. Dubosq, E. Petrishcheva, G. Bian, C. Rentenberger, C. L. Lengauer, B. Gault, G. Habler, and R. Abart, Coherent solvus of disordered alkali feldspar: Experiment, atom probe tomography and thermodynamic model, *Contributions to Mineralogy and Petrology* **179**, 68 (2024).
 - [12] F. Delbove, Excess Gibbs energy of microcline-low albite alkali feldspars at 800°C and 1 bar, based on fused alkali bromide ion-exchange experiments, *American Mineralogist: Journal of Earth and Planetary Materials* **60**, 972 (1975).
 - [13] G. L. Hovis, F. Delbove, and M. R. Bose, Gibbs energies and entropies of K-Na mixing for alkali feldspars from phase equilibrium data; implications for feldspar solvi and short-range order, *American Mineralogist* **76**, 913 (1991).
 - [14] G. Neusser, R. Abart, F. D. Fischer, D. Harlov, and N. Norberg, Experimental Na/K exchange between alkali feldspar and an NaCl–KCl salt melt: Chemically induced fracturing and element partitioning, *Contributions*

- to Mineralogy and Petrology **164**, 341 (2012).
- [15] D. Heuser, E. Petrishcheva, F. Ingegneri, C. L. Lengauer, E. Dachs, C. Hauzenberger, and R. Abart, Thermodynamic mixing properties of disordered alkali feldspar solid-solution from Na–K partitioning and low-temperature calorimetry, *Physics and Chemistry of Minerals* **51**, 9 (2024).
 - [16] H. T. Haselton, G. L. Hovis, B. S. Hemingway, and R. A. Robie, Calorimetric investigation of the excess entropy of mixing in analbite-sanidine solid solutions; lack of evidence for Na, K short-range order and implications for two-feldspar thermometry, *American Mineralogist* **68**, 398 (1983).
 - [17] L. Zhang and A. Lüttge, Al,Si order in albite and its effect on albite dissolution processes: A Monte Carlo study, *American Mineralogist* **92**, 1316 (2007).
 - [18] B. Dubacq, Thermodynamics of ordering and mixing in plagioclase feldspars: Atomistic modelling in favour of Landau theory, *Contributions to Mineralogy and Petrology* **177**, 102 (2022).
 - [19] P. Kaercher, B. Militzer, and H.-R. Wenk, Ab initio calculations of elastic constants of plagioclase feldspars, *American Mineralogist* **99**, 2344 (2014).
 - [20] A. Benisek and E. Dachs, The accuracy of standard enthalpies and entropies for phases of petrological interest derived from density-functional calculations, *Contributions to Mineralogy and Petrology* **173**, 90 (2018).
 - [21] M. A. Antonelli, M. Schiller, E. A. Schauble, T. Mittal, D. J. DePaolo, T. Chacko, E. S. Grew, and B. Tripoli, Kinetic and equilibrium Ca isotope effects in high-T rocks and minerals, *Earth and Planetary Science Letters* **517**, 71 (2019).
 - [22] Y. Li, W. Wang, Z. Wu, and S. Huang, First-principles investigation of equilibrium K isotope fractionation among K-bearing minerals, *Geochimica et Cosmochimica Acta* **264**, 30 (2019).
 - [23] A. Benisek, E. Dachs, and M. Grodzicki, First-principles investigation of the lattice vibrations in the alkali feldspar solid solution, *Physics and Chemistry of Minerals* **42**, 243 (2015).
 - [24] A. Benisek and E. Dachs, Excess enthalpy of mixing of mineral solid solutions derived from density-functional calculations, *Physics and Chemistry of Minerals* **47**, 15 (2020).
 - [25] Y. Li, W. Wang, S. Huang, K. Wang, and Z. Wu, First-principles investigation of the concentration effect on equilibrium fractionation of K isotopes in feldspars, *Geochimica et Cosmochimica Acta* **245**, 374 (2019).
 - [26] A. Gorfer, R. Abart, and C. Dellago, Structure and thermodynamics of defects in Na-feldspar from a neural network potential, *Physical Review Materials* **8**, 073602 (2024).
 - [27] P. Pedevilla, S. J. Cox, B. Slater, and A. Michaelides, Can ice-like structures form on non-ice-like substrates? The example of the K-feldspar microcline, *The Journal of Physical Chemistry C* **120**, 6704 (2016).
 - [28] T. Dickbreder, F. Sabath, B. Reischl, R. V. E. Nilsson, A. S. Foster, R. Bechstein, and A. Kühnle, Atomic structure and water arrangement on K-feldspar microcline (001), *Nanoscale* **16**, 3462 (2024).
 - [29] P. M. Piaggi, A. Selloni, A. Z. Panagiotopoulos, R. Car, and P. G. Debenedetti, A first-principles machine-learning force field for heterogeneous ice nucleation on microcline feldspar, *Faraday Discussions* **249**, 98 (2024).
 - [30] O. T. Unke, S. Chmiela, H. E. Sauceda, M. Gastegger, I. Poltavsky, K. T. Schütt, A. Tkatchenko, and K.-R. Müller, Machine learning force fields, *Chemical Reviews* **121**, 10142 (2021).
 - [31] A. Gorfer, R. Abart, and C. Dellago, Mechanism and kinetics of sodium diffusion in Na-feldspar from neural network based atomistic simulations, *arXiv:2405.19008 [cond-mat.mtrl-sci]* (2024).
 - [32] T. L. Grove, M. B. Baker, and R. J. Kinzler, Coupled CaAl–NaSi diffusion in plagioclase feldspar: Experiments and applications to cooling rate speedometry, *Geochimica et Cosmochimica Acta* **48**, 2113 (1984).
 - [33] D. J. Cherniak, Silicon self-diffusion in single-crystal natural quartz and feldspar, *Earth and Planetary Science Letters* **214**, 655 (2003).
 - [34] G. L. Hovis, Behavior of alkali feldspars; Crystallographic properties and characterization of composition and Al–Si distribution, *American Mineralogist* **71**, 869 (1986).
 - [35] D. Gehringer, M. Friák, and D. Holec, Models of configurationally-complex alloys made simple, *Computer Physics Communications* **286**, 108664 (2023).
 - [36] A. H. Larsen, J. J. Mortensen, J. Blomqvist, I. E. Castelli, R. Christensen, M. Dulak, J. Friis, M. N. Groves, B. Hammer, C. Hargus, E. D. Hermes, P. C. Jennings, P. B. Jensen, J. Kermode, J. R. Kitchin, E. L. Kolsbjerg, J. Kubal, K. Kaasbjerg, S. Lysgaard, J. B. Maronsson, T. Maxson, T. Olsen, L. Pastewka, A. Peterson, C. Rostgaard, J. Schiøtz, O. Schütt, M. Strange, K. S. Thygesen, T. Vegge, L. Vilhelmsen, M. Walter, Z. Zeng, and K. W. Jacobsen, The atomic simulation environment—a Python library for working with atoms, *Journal of Physics: Condensed Matter* **29**, 273002 (2017).
 - [37] G. Kresse and J. Hafner, Ab initio molecular dynamics for liquid metals, *Physical Review B* **47**, 558 (1993).
 - [38] G. Kresse and J. Furthmüller, Efficient iterative schemes for ab initio total-energy calculations using a plane-wave basis set, *Physical Review B* **54**, 11169 (1996).
 - [39] G. Kresse and J. Furthmüller, Efficiency of ab-initio total energy calculations for metals and semiconductors using a plane-wave basis set, *Computational Materials Science* **6**, 15 (1996).
 - [40] G. Kresse and D. Joubert, From ultrasoft pseudopotentials to the projector augmented-wave method, *Physical Review B* **59**, 1758 (1999).
 - [41] J. P. Perdew, K. Burke, and M. Ernzerhof, Generalized gradient approximation made simple, *Physical Review Letters* **77**, 3865 (1996).
 - [42] A. Gorfer, R. Abart, and C. Dellago, Structure and thermodynamics of defects in Na-feldspar from a neural network potential - Accompanying Data (2024), [Data Set] <https://doi.org/10.5281/zenodo.10630971>.
 - [43] J. Behler and M. Parrinello, Generalized neural-network representation of high-dimensional potential-energy surfaces, *Physical Review Letters* **98**, 146401 (2007).
 - [44] J. Behler, Atom-centered symmetry functions for constructing high-dimensional neural network potentials, *The Journal of Chemical Physics* **134**, 074106 (2011).
 - [45] M. Gastegger, L. Schwiedrzik, M. Bittermann, F. Berzsényi, and P. Marquetand, wACSF—Weighted atom-centered symmetry functions as descriptors in machine learning potentials, *The Journal of Chemical Physics* **148**, 241709 (2018).
 - [46] A. Singraber, J. Behler, and C. Dellago, Library-based LAMMPS implementation of high-dimensional neural

- network potentials, *Journal of Chemical Theory and Computation* **15**, 1827 (2019).
- [47] A. Singraber, T. Morawietz, J. Behler, and C. Dellago, Parallel multistream training of high-dimensional neural network potentials, *Journal of Chemical Theory and Computation* **15**, 3075 (2019).
- [48] L. Kývala, A. Angeletti, C. Franchini, and C. Dellago, Diffusion and coalescence of phosphorene monovacancies studied using high-dimensional neural network potentials, *The Journal of Physical Chemistry C* **127**, 23743 (2023).
- [49] R. Jinnouchi, F. Karsai, and G. Kresse, On-the-fly machine learning force field generation: Application to melting points, *Physical Review B* **100**, 014105 (2019).
- [50] R. Jinnouchi, J. Lahnsteiner, F. Karsai, G. Kresse, and M. Bokdam, Phase transitions of hybrid perovskites simulated by machine-learning force fields trained on the fly with Bayesian Inference, *Physical Review Letters* **122**, 225701 (2019).
- [51] A. P. Thompson, H. M. Aktulga, R. Berger, D. S. Bolinteanu, W. M. Brown, P. S. Crozier, P. J. in 't Veld, A. Kohlmeyer, S. G. Moore, T. D. Nguyen, R. Shan, M. J. Stevens, J. Tranchida, C. Trott, and S. J. Plimpton, LAMMPS - a flexible simulation tool for particle-based materials modeling at the atomic, meso, and continuum scales, *Computer Physics Communications* **271**, 108171 (2022).
- [52] A. Gorfer, D. A. Heuser, R. Abart, and C. Dellago, Thermodynamics of alkali feldspar solid solutions with varying Al-Si order: Atomistic simulations using a neural network potential - Accompanying Data (2024), [Data Set] <https://doi.org/10.5281/zenodo.12801605>.
- [53] B. Sadigh, P. Erhart, A. Stukowski, A. Caro, E. Martinez, and L. Zepeda-Ruiz, Scalable parallel Monte Carlo algorithm for atomistic simulations of precipitation in alloys, *Physical Review B* **85**, 184203 (2012).
- [54] R. J. Angel, N. L. Ross, J. Zhao, L. Sochalski-Kolbus, H. Krüger, and B. C. Schmidt, Structural controls on the anisotropy of tetrahedral frameworks: The example of monoclinic feldspars, *European Journal of Mineralogy* **25**, 597 (2013).
- [55] D. R. Allan and R. J. Angel, A high-pressure structural study of microcline (KAlSi₃O₈) to 7 GPa, *European Journal of Mineralogy* **9**, 263 (1997).
- [56] J. M. Brown, E. H. Abramson, and R. J. Angel, Triclinic elastic constants for low albite, *Physics and Chemistry of Minerals* **33**, 256 (2006).
- [57] E. Petrishcheva, D. Heuser, and R. Abart, Coherent lamellar intergrowth in alkali feldspar, *Contributions to Mineralogy and Petrology* **178**, 77 (2023).
- [58] C. Wolverton, V. Ozolins, and A. Zunger, Short-range-order types in binary alloys: A reflection of coherent phase stability, *Journal of Physics: Condensed Matter* **12**, 2749 (2000).
- [59] C. Wolverton, V. Ozoliņš, and A. Zunger, First-principles theory of short-range order in size-mismatched metal alloys: Cu-Au, Cu-Ag, and Ni-Au, *Physical Review B* **57**, 4332 (1998).
- [60] M. Muzyk, D. Nguyen-Manh, K. J. Kurzydłowski, N. L. Baluc, and S. L. Dudarev, Phase stability, point defects, and elastic properties of W-V and W-Ta alloys, *Physical Review B* **84**, 104115 (2011).
- [61] R. A. Swalin, Thermodynamic properties of alloy systems—A model approach, in *Thermodynamics of Solids*, Wiley Series on the Science and Technology of Materials (Wiley, 1972) 2nd ed., pp. 141–164.
- [62] J. Behler, Four generations of high-dimensional neural network potentials, *Chemical Reviews* **121**, 10037 (2021).
- [63] Y. Kumagai and F. Oba, Electrostatics-based finite-size corrections for first-principles point defect calculations, *Physical Review B* **89**, 195205 (2014).
- [64] M. Gajdoš, K. Hummer, G. Kresse, J. Furthmüller, and F. Bechstedt, Linear optical properties in the projector-augmented wave methodology, *Physical Review B* **73**, 045112 (2006).

SUPPLEMENTAL MATERIAL

A. System snapshots

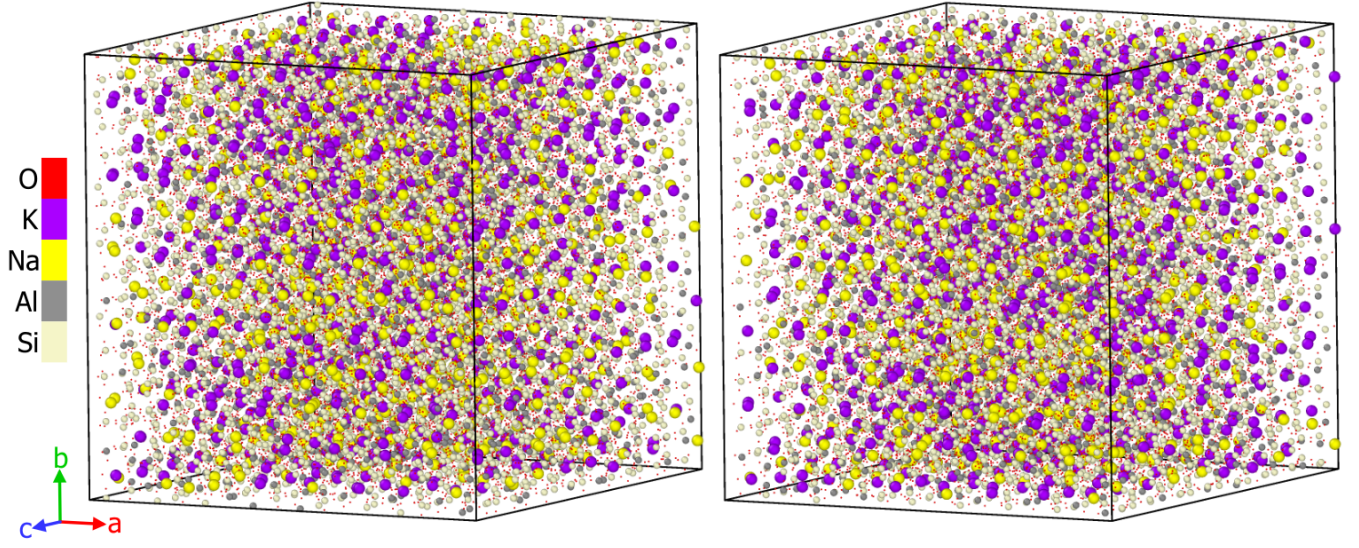


Figure S-1. Snapshots of the Al disordered alkali feldspar during the SGCMC-MD at 1073.15 K for $\Delta\mu = -0.021875$ eV. The two snapshots are 160 ps or 100 000 attempted and 26 576 accepted MC moves apart.

B. Functional fits

1. Figure 4 and Figure 5 (b)

The chemical potential versus X_K , computed using the SGCMC-MD and shown in Figure 4 (a), was fitted with

$$\Delta\mu = k_B T \log \left[\frac{X_K}{1 - X_K} \right] + \sum_{i=0}^n A_i X_K^i, \quad (\text{S-1})$$

where we used a third order polynomial, i.e. $n = 3$. The Gibbs energies of mixing of Figure 4 (b) were then determined by

$$g^{\text{mix}} = k_B T (X_K \log X_K + (1 - X_K) \log [1 - X_K]) + \sum_{i=0}^n \frac{A_i X_K^{i+1}}{i+1} - X_K \sum_{i=0}^n \frac{A_i}{i+1}, \quad (\text{S-2})$$

where the first two terms are just the integral of Eq. S-1 and in the last we subtract the linear dependency. If we leave out the first term, the ideal Gibbs free energy without linear dependency, we get the excess Gibbs free energy of mixing:

$$g^{\text{ex}} = \sum_{i=0}^n \frac{A_i X_K^{i+1}}{i+1} - X_K \sum_{i=0}^n \frac{A_i}{i+1}, \quad (\text{S-3})$$

shown in Fig. 5 (b).

2. Figure 5 (a,c) - Margules mixing model

The excess enthalpy of mixing h^{ex} and the excess entropy of mixing s^{ex} (but not the g^{ex}) were fitted using a Margules mixing model

$$\begin{aligned} h^{\text{ex}} &= X_K(1 - X_K) [W_{hK}(1 - X_K) + W_{hNa}X_K] \\ s^{\text{ex}} &= X_K(1 - X_K) [W_{sK}(1 - X_K) + W_{sNa}X_K], \end{aligned} \quad (\text{S-4})$$

yielding the Margules parameters W_{hK}, W_{hNa}, W_{sK} and W_{sNa} given in Table II. Equation S-3 is not of the Margules form, but we can use the relation

$$W_g = W_h - W_s T, \quad (\text{S-5})$$

to also determine W_{gK} and W_{gNa} .

C. Special weighted atom centered symmetry functions

The Atom Centered Symmetry Functions (ACSF) introduced in [43, 44] are the two-body or radial ACSF G_i^2 and the three-body or angular ACSF; narrow angular G_i^3 and wide angular G_i^9 :

$$\begin{aligned} G_i^2 &= \sum_{j \neq i} \exp[-\eta(r_{ij} - r_s)^2] f_c(r_{ij}) \\ G_i^3 &= 2^{1-\zeta} \sum_{j, k \neq i, j < k} (1 + \lambda \cos \theta_{ijk})^\zeta \exp[-\eta((r_{ij} - r_s)^2 + (r_{ik} - r_s)^2 + (r_{jk} - r_s)^2)] f_c(r_{ij}) f_c(r_{ik}) f_c(r_{jk}), \\ G_i^9 &= 2^{1-\zeta} \sum_{j, k \neq i, j < k} (1 + \lambda \cos \theta_{ijk})^\zeta \exp[-\eta((r_{ij} - r_s)^2 + (r_{ik} - r_s)^2)] f_c(r_{ij}) f_c(r_{ik}), \end{aligned}$$

where r_{ij} is the distance vector between the central atom i and its neighbor j , η is a hyperparameter for the shape of the Gaussians, λ centers the cosine terms at the three-body angle θ_{ijk} at 0 deg or 180 deg, $2^{1-\zeta}$ is a normalization factor, r_s shifts the center of the Gaussians and f_c is a smooth cutoff function. We refer to Ref. [62] for more details and note that the above equations use the notation of n2p2 [46].

Chemically diverse systems can pose a challenge when using the angular ACSF as the number of combinations of elements grows quadratically with number of chemical elements such that around five elements the use of ACSF becomes computationally unwieldy. An alternative symmetry function type to amend this issue was introduced by Gastegger et al. [45] in the form of weighted ACSF W^3 in which an additional prefactor $h(A_j, B_k)$ is introduced inside the sum of G_i^3 :

$$W_i^3 = 2^{1-\zeta} \sum_{j, k \neq i, j < k} h(A_j, B_k) (1 + \lambda \cos \theta_{ijk})^\zeta \exp(-\eta((r_{ij} - r_s)^2 + (r_{ik} - r_s)^2 + (r_{jk} - r_s)^2)) f_c(r_{ij}) f_c(r_{ik}) f_c(r_{jk})$$

where A_j, B_k are the atom-types for one pair of neighbors. In [45] the function $h(A_j, B_k)$ was identified with:

$$h^Z(A_j, B_k) \equiv Z_j Z_k,$$

where Z is the atomic number. After preliminary tests in using h^Z for the construction of the NNP for alkali feldspar (O Al Si Na K) we were prompted to search for alternative definitions of $h(A_j, B_k)$.

After multiple trials of different definitions the best performing choice was the use of G_i^3 and G_i^9 for angles involving O together with W_i^3 where h is:

$$h^x(A_j, B_k) \equiv \chi_j \chi_k,$$

where χ is the Pauling electronegativity. For example,

$$h^x(\text{Na}, \text{Al}) = 0.92 \cdot 1.61 = 1.48$$

We believe this is a reasonable choice of h as χ is certainly a better signifier of chemical uniqueness than Z and suspect that this could be a better choice of $h(A_j, B_k)$ in general.

D. Electrostatic correction for charged defects

The inclusion of charged defects in the training data warrants the use of corrections to mitigate electrostatic finite size effects. To the potential energies that result from DFT calculations, we therefore added a correction term. This was explored in our previous study [26], where we used the Kumagai and Oba correction. That correction is however not feasible to do for the present NNP as one would formally need to determine a different correction for every realization of Al-Si and Na-K disorder. The point charge correction E_{PC} was used instead.

To calculate the correction we need the Madelung potential for a charge q at $\mathbf{r} = \mathbf{0}$ for a general anisotropic dielectric tensor $\bar{\epsilon}$ [63] (Eq. 8):

$$\begin{aligned} V_{\text{PC},q}^{\text{aniso}}(\mathbf{r} = \mathbf{0}) = & \sum_{\mathbf{R}_i}^{i \neq 0} \frac{q}{\sqrt{|\bar{\epsilon}|}} \frac{\text{erfc}\left(\gamma \sqrt{\mathbf{R}_i \cdot \bar{\epsilon}^{-1} \cdot \mathbf{R}_i}\right)}{\sqrt{\mathbf{R}_i \cdot \bar{\epsilon}^{-1} \cdot \mathbf{R}_i}} - \frac{\pi q}{\Omega \gamma} \\ & + \sum_{\mathbf{G}_i}^{i \neq 0} \frac{4\pi q}{\Omega} \frac{\exp(-\mathbf{G}_i \cdot \bar{\epsilon} \cdot \mathbf{G}_i / 4\gamma^2)}{\mathbf{G}_i \cdot \bar{\epsilon} \cdot \mathbf{G}_i} - \frac{2\gamma q}{\sqrt{\pi|\bar{\epsilon}|}}, \end{aligned}$$

where \mathbf{R}_i are lattice vectors, \mathbf{G}_i are reciprocal lattice vectors, \mathbf{R}_0 and \mathbf{G}_0 are $\mathbf{0}$, γ is a convergence parameter and Ω the supercell volume.

Then the point charge correction is given by:

$$E_{\text{PC}} = -\frac{q}{2} V_{\text{PC},q}^{\text{aniso}}(\mathbf{r} = \mathbf{0}).$$

The charge depends on the inserted defect. For the case of the interstitial defects (Na-Na-dumbbell, Na-(0,0, $\frac{1}{2}$)-interstitial, Na-K-dumbbell) q has a value of +1. For the case of the vacancies (Na-vacancy and K-vacancy) q has a value of -1. For the case of the defect-free system, no correction is necessary, i.e. q has a value of 0.

The dielectric tensor $\bar{\epsilon}$ is a material-dependent property. We do not consider Al-Si disorder effects on the dielectric tensor. For the case of ordered pure Na-feldspar, the dielectric tensor $\bar{\epsilon}_{\text{Na}}$ was calculated from DFT in [26]. Here we repeated the same DFT perturbation routines implemented in VASP [64] for ordered pure K-feldspar, yielding the $\bar{\epsilon}_{\text{K}}$.

The dielectric tensor for intermediate Na-K compositions X_{K} was then approximated using the interpolation

$$\bar{\epsilon}(X_{\text{K}}) = (1 - X_{\text{K}})\bar{\epsilon}_{\text{Na}} + X_{\text{K}}\bar{\epsilon}_{\text{K}}.$$